



OPEN ACCESS

EDITED BY

Jingfeng Jiang,
Michigan Technological University,
United States

REVIEWED BY

Md. Ashikuzzaman,
Johns Hopkins University, United States
Lin Qi,
Northeastern University, China
He Li,
Vinnno Technology Co., Ltd., China

*CORRESPONDENCE

Vera H. J. van Hal,
✉ v.h.j.v.hal@tue.nl

RECEIVED 12 October 2023

ACCEPTED 12 February 2024

PUBLISHED 28 March 2024

CITATION

van Hal VHJ, de Hoop H, van Sambeek MRHM,
Schwab H-M and Lopata RGP (2024), *In vivo*
bistatic dual-aperture ultrasound imaging and
elastography of the abdominal aorta.
Front. Physiol. 15:1320456.
doi: 10.3389/fphys.2024.1320456

COPYRIGHT

© 2024 van Hal, de Hoop, van Sambeek,
Schwab and Lopata. This is an open-access
article distributed under the terms of the
[Creative Commons Attribution License \(CC
BY\)](https://creativecommons.org/licenses/by/4.0/). The use, distribution or reproduction in
other forums is permitted, provided the
original author(s) and the copyright owner(s)
are credited and that the original publication
in this journal is cited, in accordance with
accepted academic practice. No use,
distribution or reproduction is permitted
which does not comply with these terms.

In vivo bistatic dual-aperture ultrasound imaging and elastography of the abdominal aorta

Vera H. J. van Hal^{1*}, Hein de Hoop¹, Marc R. H. M. van
Sambeek^{1,2}, Hans-Martin Schwab¹ and Richard G. P. Lopata¹

¹Photoacoustics and Ultrasound Laboratory Eindhoven (PULS/e), Department of Biomedical Engineering, Eindhoven University of Technology, Eindhoven, Netherlands, ²Department of Vascular Surgery, Catharina Hospital, Eindhoven, Netherlands

Introduction: In this paper we introduce *in vivo* multi-aperture ultrasound imaging and elastography of the abdominal aorta. Monitoring of the geometry and growth of abdominal aortic aneurysms (AAA) is paramount for risk stratification and intervention planning. However, such an assessment is limited by the lateral lumen-wall contrast and resolution of conventional ultrasound. Here, an *in vivo* dual-aperture bistatic imaging approach is shown to improve abdominal ultrasound and strain imaging quality significantly. By scanning the aorta from different directions, a larger part of the vessel circumference can be visualized.

Methods: In this first-in-man volunteer study, the performance of multi-aperture ultrasound imaging and elastography of the abdominal aortic wall was assessed in 20 healthy volunteers. Dual-probe acquisition was performed in which two curved array transducers were aligned in the same imaging plane. The transducers alternately transmit and both probes receive simultaneously on each transmit event, which allows for the reconstruction of four ultrasound signals. Automatic probe localization was achieved by optimizing the coherence of the trans-probe data, using a gradient descent algorithm. Speckle-tracking was performed on the four individual bistatic signals, after which the respective axial displacements were compounded and strains were calculated.

Results: Using bistatic multi-aperture ultrasound imaging, the image quality of the ultrasound images, *i.e.*, the angular coverage of the wall, was improved which enables accurate estimation of local motion dynamics and strain in the abdominal aortic wall. The motion tracking error was reduced from 1.3 mm \pm 0.63 mm to 0.16 mm \pm 0.076 mm, which increased the circumferential elastographic signal-to-noise ratio (SNRe) by 12.3 dB \pm 8.3 dB on average, revealing more accurate and homogeneous strain estimates compared to single-perspective ultrasound.

Conclusion: Multi-aperture ultrasound imaging and elastography is feasible *in vivo* and can provide the clinician with vital information about the anatomical and mechanical state of AAAs in the future.

KEYWORDS

abdominal aorta, elastography, multi-aperture, ultrasound, coherent compounding

1 Introduction

Ultrasound imaging is widely used in clinical practice to monitor the size and growth of abdominal aortic aneurysms (Wanhainen et al., 2020). When the aortic diameter exceeds 5.0 cm in women and 5.5 cm in men, or when the growth rate exceeds 1 cm/year, surgical intervention is performed (Wanhainen et al., 2020). However, this threshold is based on population statistics (Brewster et al., 2003), and previous studies have highlighted the limitation of purely morphological assessment for the estimation of the rupture risk (Darling et al., 1977; Raut et al., 2013). The knowledge of the full aneurysm geometry as well as the wall motion dynamics and strain can give valuable insights in the mechanical state of the abdominal aortic wall, and contribute to a more patient-specific rupture risk assessment (Bihari et al., 2013; Karatolios et al., 2013; Wittek et al., 2013; Van Disseldorp et al., 2016).

However, the use of conventional ultrasound for the reconstruction of aortic geometry and estimation of wall motion and strain has its limitations. Tissue interfaces perpendicular to the propagation direction of the ultrasound wave reflect well, whereas at interfaces parallel to the propagation direction the ultrasound wave may reflect away from the transducer (Pettersen et al., 2021). As a result, the anterior and posterior side of the vessel wall can be well visualized by the specular reflections, but there is limited to poor contrast and resolution at the lateral sides. This is also illustrated in (Matthews et al., 2021), where it is shown that the reproducibility of aortic diameter measurements in the transverse direction is significantly lower compared to the anterior-posterior plane. To overcome these physical limitations of ultrasound imaging, the aorta can be scanned from multiple directions to increase the visibility of the entire circumference of the aortic wall by specular reflections. In Pettersen et al. (2021), this concept of multi-perspective ultrasound imaging, in which an ultrasound probe was physically translated over the abdomen, improved lateral contrast of the abdominal aorta in healthy volunteers. In a later study (Sjoerdsma et al., 2023), 3D multi-perspective ultrasound imaging was also performed in patients with an abdominal aortic aneurysm. Also in obstetric (Zimmer et al., 2023) and cardiac applications (Rajpoot et al., 2011; Mulder et al., 2014), the use of multi-perspective imaging has shown to improve the visibility of the imaged structures. However, in such an approach, the ultrasound images have to be temporally aligned to match the cardiac cycle. This can be problematic because of the changes in the hemodynamics between acquisitions.

Recent developments in ultrafast imaging (Tanter and Fink, 2014) have enabled the use of multiple apertures during one acquisition, by performing interleaved scanning (Peralta et al., 2019; de Hoop et al., 2020; Liu et al., 2022a), or in a configuration that enables the transmission of one coherent wavefront using all apertures at the same time (Foiret et al., 2022). In these studies, multiple linear or curved array transducers were used, typically driven by research ultrasound platforms, to develop the multi-aperture imaging systems. Dual-aperture ultrasound also allows for bistatic imaging, a concept that originates from radar technology (Burkholder et al., 2003), in which one transducer transmits and a second transducer receives. This concept has previously also been used in for instance Doppler

imaging, to obtain more reliable velocity estimates (Dunmire et al., 2000). In (Van Hal et al., 2021), dual-aperture bistatic ultrasound imaging of the abdominal aorta allowed for the reconstruction of four ultrasound signals, since both transducers received simultaneously upon each transmit event. Using this dual-receive image acquisition configuration, the visibility of the aortic wall circumference in simulations and *ex vivo* porcine aortas was increased by 200%.

Multi-aperture ultrasound imaging cannot only improve ultrasound image quality, but it can also improve the assessment of tissue deformation and strain (Van Hal et al., 2021; Liu et al., 2022b). Conventional strain imaging techniques are limited by the lack of phase information and resolution in the lateral direction of the ultrasound beam (Lopata et al., 2009b; Hansen et al., 2010). Phase information in the lateral direction can be added by the use of beam steering (Techavipoo et al., 2004; Hansen et al., 2010), however, this technique cannot be applied to the abdominal aorta or deeper lying structures in general, considering the limited overlapping region in compounding at large depths (Pettersen et al., 2021). This insufficient overlap can be overcome by the use of multiple probes, as shown in (Van Hal et al., 2021; Liu et al., 2022b). The addition of the second transducer improved accuracy and precision of radial and circumferential strain estimates in aortic and cardiac applications. However, so far all these studies were conducted in *ex vivo* experiments. *In vivo* application of ultrafast multi-aperture ultrasound imaging have been shown in (Peralta et al., 2020; Foiret et al., 2022), in which its performance in terms of increased field-of-view (FOV) and improved resolution was shown in the liver of a healthy volunteer.

In this study, the advantage of using multiple apertures over conventional single-transducer imaging of the abdominal aorta is assessed *in vivo* in 22 healthy volunteers. The image quality of bistatic multi-aperture ultrasound imaging is compared to single-perspective ultrasound imaging, focusing on the visibility of the abdominal aortic wall and surrounding tissues. Moreover, bistatic multi-aperture strain imaging is performed *in vivo* for the first time to assess the improvement in the estimation of wall motion and strain. *In vivo* evaluation of the developed algorithms for image reconstruction, image registration and fusion, and strain imaging is important since physical conditions will be different and more challenging than those experienced in experimental and simulated set-ups. For instance, there are additional challenges considering the larger imaging depth and speed-of-sound differences in the abdominal wall. This also makes accurate estimation of the probe positions more difficult, which is essential for the reconstruction and fusion of multi-aperture bistatic ultrasound images. In previous research, probe localization relied on detectable and isolated point scatterers (Peralta et al., 2019), inherent image features (Pettersen et al., 2021) or the reflection coming from the lens of the second transducer (De Hoop et al., 2020; Van Hal et al., 2021). We have now developed a more generic method for probe localization, based on maximizing signal coherence. Finally, our set-up allowed for flexible positioning of the probes, to obtain the best probe angle for each individual subject based on the acquired images. The influence of this relative probe positioning on the ultrasound image quality is also investigated.

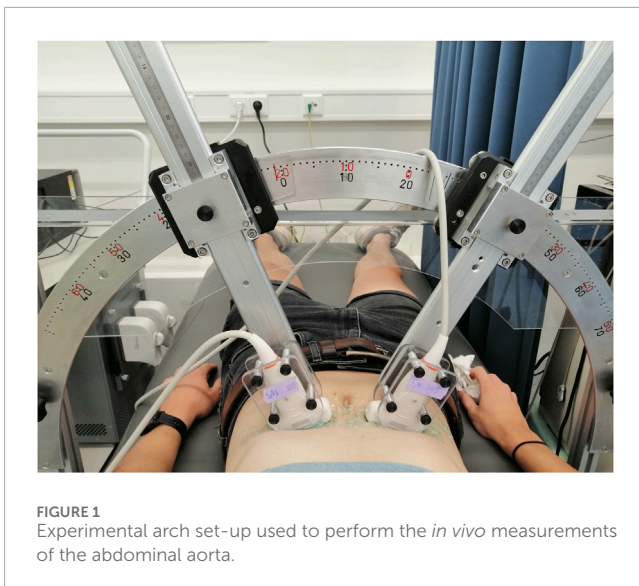


FIGURE 1
Experimental arch set-up used to perform the *in vivo* measurements of the abdominal aorta.

2 Materials and methods

2.1 Ultrasound acquisition

The feasibility and performance of bistatic multi-aperture ultrasound imaging and strain imaging of the abdominal aorta was tested in 22 healthy volunteers, between 18–60 years of age. The experiment protocol was approved by the ethical review board of the Eindhoven University of Technology and written informed consent was obtained prior to scanning. Measurements were performed using the Verasonics Vantage 256 (Kirkland, Seattle, WA, United States), equipped with two C5-2v curved array transducers with a center frequency of 3.7 MHz. A customized arch was designed on which the probe holders were attached (Figure 1). This mechanical arch allows for free positioning of the probes under a certain angle, while keeping them in the same imaging plane. After adjusting for the optimal position of the transducers, based on the images acquired, the data were recorded for approximately 3 cardiac cycles during breath-hold. The acquisition parameters for dual-aperture ultrafast imaging were based on the experiences in (Van Hal et al., 2021) and chosen according to a trade-off between the image quality and frame rate (Alomari et al., 2014), and to prevent signal decorrelation between the two transducers. An interleaved acquisition scheme was used using 15 diverging waves per transducer with a pulse repetition frequency of 4 kHz. Hence, the time between transducers was equal to 3.75 ms. Transmit apodization by a Tukey window was applied to all transducer elements to reduce the intensity of the side-lobes. The transmit angles, defined as the angle of the transmit beam with the z-axis at the location of the transducer origin, were set between -12° and 12° . The resulting frame rate for each transducer was equal to 130 Hz. The acquisition parameters are summarized in Table 1.

The mechanical safety of the ultrafast acquisition schemes was guaranteed, by measuring the mechanical index (MI), spatial peak pulse average intensity (I_{SPPA}), and spatial peak time average intensity (I_{SPTA}) using a dedicated water tank system (Precision

TABLE 1 Acquisition parameters.

Setting	Value
Center frequency C5-2v probe	3.7 MHz
Steering angles	$[-12^\circ, 12^\circ]$
Frame rate	130 Hz
Pulse repetition frequency	4 kHz
Number of transmits per probe	15

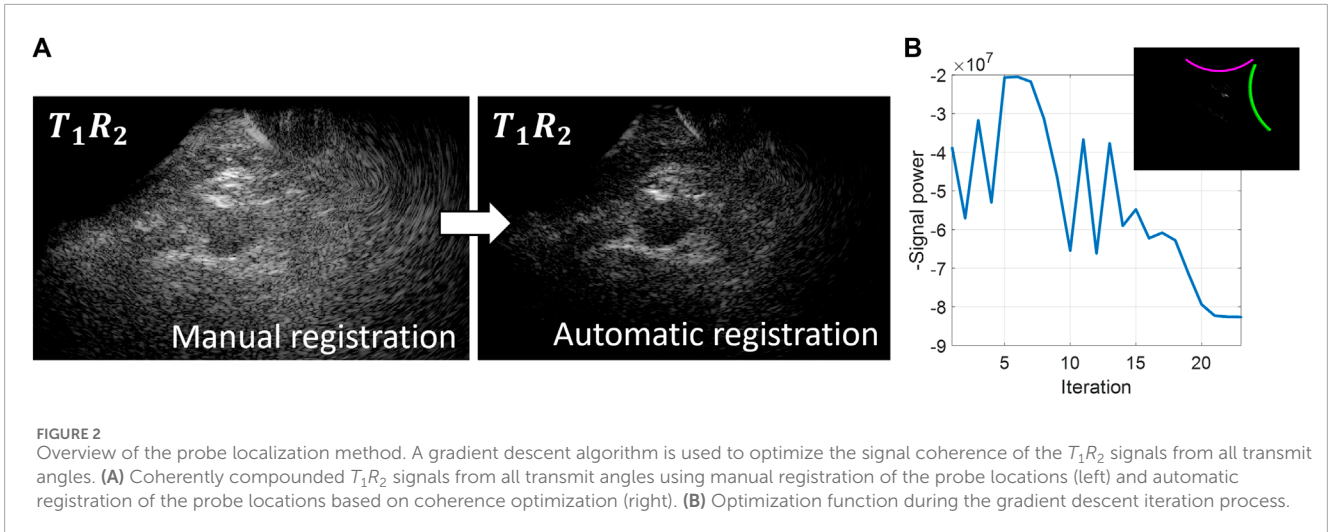
Acoustics Ltd, Dorchester, UK). A hydrophone (Onda HNP-0400) was used to measure acoustic pressure, and could be positioned at any desired measurement location using the UMS Control Software. The measurements were performed for different transmit voltages, steering angles, pulse repetition and transmit frequencies. The results were compared against the FDA limits for abdominal ultrasound imaging after deration at a rate of 0.3 dB/cm/MHz. Moreover, the surface temperature of the curved array transducer was monitored in free air and on a test object, according to IEC 60601-2-37 (NEN-EN-IEC 60601-2-37:2008/A1:2015, 2015). All values used in this study are under the FDA regulatory limits for MI of 1.9, I_{SPPA} of 190 W/cm^2 and I_{SPTA} of 94 mW/cm^2 . Furthermore, there were no limits for the maximum scanning time according to the surface temperature measurements. For interleaved dual-transducer imaging, the same regulatory limits apply as for conventional ultrasound imaging, since only one transducer is active at the same time.

2.2 Image registration and fusion

Registration and fusion of the images from the two ultrasound probes was performed in postprocessing after the acquisition of the ultrasound data. All image processing operations were performed in MATLAB 2021a (The MathWorks, Natick, MA, United States). In order to align the ultrasound images from the two probes and for the reconstruction of the signals transmitted by one transducer and received by the other transducer (the trans-probe data), accurate probe localization is essential. For this purpose, the IQ data were reconstructed on a Cartesian grid with a spacing of $\frac{1}{2}$ wavelength (λ) in both directions.

The probe localization method is based on maximizing the signal coherence of the compounded T_1R_2 signals from all transmit angles. Since the coherence optimization therefore focuses both in transmit and receive, it can be expected that the signal power increases towards the correct probe positions. The negative signal power was used as the objective function for a gradient descent algorithm to find the optimum geometric transformation T , parameterized by two translational and one rotational degree of freedom. The definition of the negative signal power P^- is given in Eq. 1, where N is the number of pixels in the imaged region, and A_i the amplitude of a pixel in the envelope detected T_1R_2 image.

$$P^- = - \sum_{i=1}^N |A_i|^2 \quad (1)$$



An overview of the probe localization method is provided in [Figure 2](#). The numerical gradient was evaluated in each of the three degrees of freedom simultaneously, to update the estimated probe positions from the previous iteration by multiplying it with learning rate μ (Eq. 2).

$$\mathbf{T} \leftarrow \mathbf{T} - \mu \nabla_{\mathbf{T}} (P^-(\mathbf{T})) \quad (2)$$

Initialization of the gradient descent algorithm was performed using the probe angle that could be read from the customized arch. After rotating the images based on this probe angle, the images from the two probes were registered manually based on the location of the aorta to obtain the initial translation parameters. As can be seen in [Figure 2](#), these initial registration parameters did not result in optimum image quality and signal power of the T_1R_2 image. During the gradient descent optimization process, the image quality of the T_1R_2 image is improved. Convergence of the gradient descent algorithm was determined by the value of the negative signal power. Convergence was achieved when the negative signal power remained constant (within a 5% range of the difference compared to the starting value) for a minimum of 3 iterations. Since initialization was performed by manual registration of the images, less than 50 iterations were needed for the gradient descent algorithm to converge to the optimum relative probe positions. Using a GPU-accelerated framework for the delay-and-sum beamforming on a NVIDIA GeForce GTX 1650[®], the registration parameters were obtained in the order of 10–20 min.

After obtaining the relative probe positions, the individual four signals in bistatic ultrasound imaging were combined by means of coherent compounding on a grid with a spacing of $\frac{1}{4}\lambda$, using Eq. 3.

$$I_{bistatic} = I_{T_1R_1} + I_{T_2R_2} + \frac{1}{2} (I_{T_1R_2} + I_{T_2R_1}) \quad (3)$$

Here, T indicates the transmitting transducer, that is either 1 or 2 and R indicates the receiving transducer, that is either 1 or 2. The two trans-probe signals, which are the signals transmitted by one transducer and received by the other transducer, *i.e.*, T_1R_2 and T_2R_1 , contain similar information because of acoustic reciprocity ([Devaney, 2012](#)), therefore their relative contribution was averaged before summation with the single-probe signals (T_1R_1 and T_2R_2).

2.3 Bistatic multi-aperture strain imaging

For the purpose of displacement estimation, the received IQ data were reconstructed on a sector grid with respect to the receiving transducer. It consisted of 2 lines per pitch in the lateral direction (pixel spacing between 0.41–0.54 mm/pixel, depending on the imaging depth), and a pixel spacing of $\frac{1}{8}\lambda$ (0.051 mm/pixel) in the axial direction. With curved array transducers, the sector grid is the preferred reconstruction grid, since it allows for the estimation of displacements along the ultrasound beam direction.

Frame-to-frame displacement estimation was performed on the individual four signals using a 2-D coarse-to-fine speckle-tracking algorithm ([Lopata et al., 2009b](#)). Similar to ([Van Hal et al., 2021](#)), the coarse displacements were estimated on the envelope data, using a kernel size of 2.6 mm \times 4.5–5.9 mm (axial \times lateral). Secondly, the fine displacements were estimated on the RF-data using a kernel size of 0.8 mm \times 2.1–2.7 mm. The axial kernel sizes were determined with respect to the wall thickness of the aorta. The coarse axial kernel size was set to cover the full wall thickness, while the fine kernel size was set to approximately half the wall thickness to be able to measure radial strain. The lateral kernel size was set to be at least as large as the estimated lateral resolution at the highest tracking depth [around 2.5 mm ([Van Hal et al., 2023](#))], to include enough characteristic image features for motion tracking ([De Hoop et al., 2020](#)). These are much larger than the axial kernel sizes because of the limited resolution in this direction. The search area was defined to be 3.0 mm \times 4.9–6.5 mm for the coarse displacements and 1.0 mm \times 2.5–3.2 mm for the fine displacements. Sub-resolution displacement estimations were improved by parabolic interpolation of the cross-correlation function ([Céspedes et al., 1995](#); [Lopata et al., 2009b](#)).

As a last step, the axial and lateral displacements were filtered with a median filter of 0.6 mm \times 4.5–5.9 mm (11 \times 11 pixels).

The axial displacement fields u_{ax} were radially projected according to $u_{rad} = u_{ax}/\cos\theta$, in which θ represents the angle between the axial direction of the ultrasound transducer and the radial direction of the aorta ([Hansen et al., 2010](#)). The radial displacements were then compounded using the angular compounding technique presented in ([Hansen et al., 2010](#);

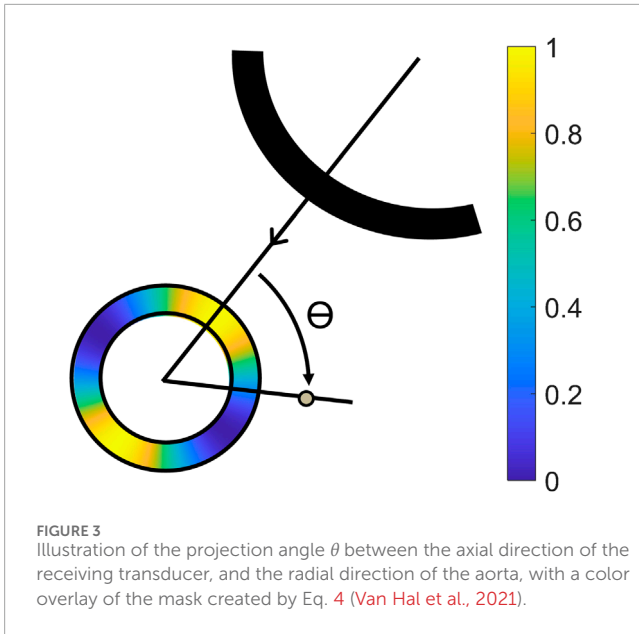


FIGURE 3 Illustration of the projection angle θ between the axial direction of the receiving transducer, and the radial direction of the aorta, with a color overlay of the mask created by Eq. 4 (Van Hal et al., 2021).

De Hoop et al., 2020; Van Hal et al., 2021). The lateral displacements were not used because of the poor lateral resolution, and the lack of phase information in this direction. Eq. 5 describes the formula that was used to weigh the radial displacement fields u_{rad} from each of the four signals in bistatic imaging. Angular weighted normalized masks \widehat{M} were defined to retrieve the most accurate displacement estimations from each ultrasound signal. The masks were created using a cosine function (De Hoop et al., 2020; Van Hal et al., 2021), and the result is illustrated in Figure 3:

$$M_{ij} = \frac{1}{2} \cos(2\theta_{ij}) + \frac{1}{2}. \quad (4)$$

Cut-out regions between the 70° and 110° angle were used to prevent infinite radial displacements. The masks were aligned with the axial direction of the receiving transducer in T_1R_1 and T_2R_2 , and the wall segments between the transducers in T_1R_2 and T_2R_1 . Again, the radial displacements fields from T_1R_2 and T_2R_1 were averaged, because these signals contain similar image information.

$$u_{rad} = \widehat{M}_{T_1R_1}(u_{rad,T_1R_1}) + \widehat{M}_{T_2R_2}(u_{rad,T_2R_2}) + \frac{1}{2}\widehat{M}_{T_1R_2}(u_{rad,T_1R_2}) + \frac{1}{2}\widehat{M}_{T_2R_1}(u_{rad,T_2R_1}) \quad (5)$$

The resulting compounded displacement field was applied to a segmentation of the vessel wall to track the wall motion over all frames. The vessel wall segmentation was created by manual segmentation of the lumen-wall border on the bistatic ultrasound image. The corresponding points on the outer border were found by extrapolating the selected points with a uniform wall thickness of 1.7 mm, based on estimations from previous research (Slobodin et al., 2016).

Finally, for the estimation of the strains, the displacements of the tracked vessel wall coordinates were calculated with respect to the first frame, after which a 2D least-squares strain estimator, described in Lopata et al. (Lopata et al., 2009a) was applied using a strain kernel of 5 radial \times 5 circumferential mesh points (1.7 mm \times 2.6 mm).

2.4 Data analysis

The generalized contrast-to-noise ratio (gCNR) (Rodriguez-Molares et al., 2019) was computed as a robust measure for the contrast between the lumen and the vessel wall. A binary mask of the vessel wall segmentation was used as ROI for the vessel wall. The lumen ROI was also created using the coordinates of the lumen-wall segmentation. However, the binary mask was eroded by a disk-shaped structuring element with a radius of 0.6 mm to ensure that the specular reflections from the vessel wall were not included. For the calculation of the gCNR, the envelope detected image data were used.

The ROI of the vessel wall was divided in 8 sections of 45° , to allow for a regional analysis of the gCNR across the vessel's circumference. Region 1 and region 5 were defined to be aligned with the beam direction of the right transducer. The signals transmitted and received by this transducer were also used as single-perspective configuration for comparison. The other regions were defined in a clockwise manner.

For the analysis of the tracking performance, the mean drift error (ME) was used. This error was calculated as the distance between the n points in the middle wall layer of the vessel segmentation at the start and the end of a complete cardiac cycle, at end-diastole. With a higher precision of the estimated displacements, the ME decreases, since the aortic wall comes back to the same position after tracking one cardiac cycle. The ME is defined in Eq. 6, where x_i and z_i denote the positions in the aortic wall at the starting frame, i.e., first end-diastole or begin systole (bs) and ending frame, i.e., second end-diastole (ed). These two frames were selected from the M-mode of the acquired ultrasound frames.

$$ME = \frac{1}{n} \sum_{i=1}^n \sqrt{(x_{i,bs} - x_{i,ed})^2 + (z_{i,bs} - z_{i,ed})^2} \quad (6)$$

The strain estimation precision was quantified by the elastographic signal-to-noise ratio (SNRe), defined by Eq. 7, using the mean (μ_ϵ) and the standard deviation (σ_ϵ) of the radial and circumferential strain estimates as measured in the middle layer of the segmented wall. This value is expected to be larger in the regional analysis of the results, compared to the global results, since a natural variation is also present in a completely correct estimation due to the spine's influence, which will lower the SNRe.

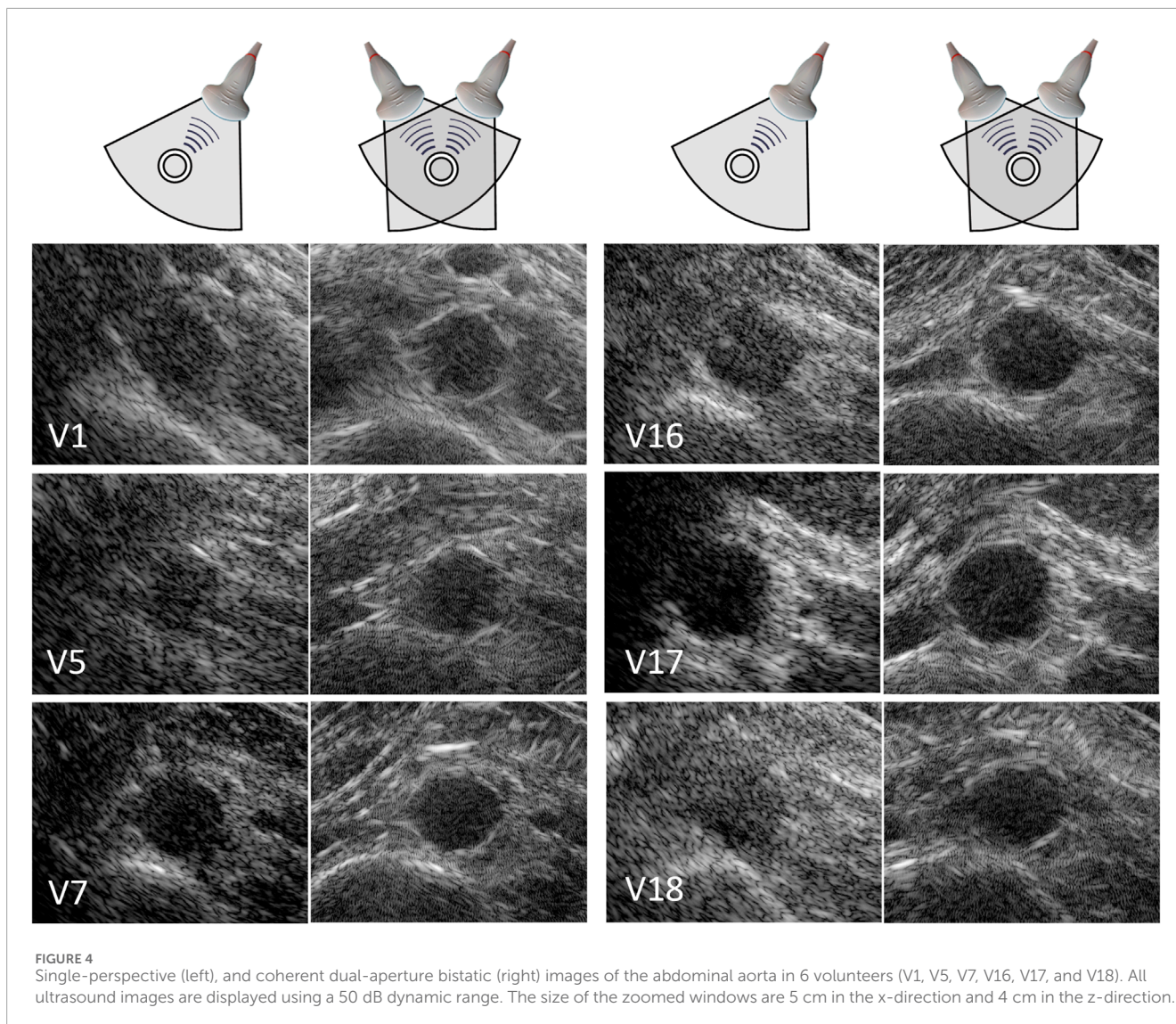
$$SNR_\epsilon = 20 \log_{10} \frac{\mu_\epsilon}{\sigma_\epsilon} \quad (7)$$

In the evaluation of the strain results, a small section (ranging between 35° and 40° wide) of the vessel wall segmentation at the left and right wall were left out, because in these regions the bistatic technique still does not add sufficient signal and contrast is low.

To compare the means of these metrics between single-perspective and bistatic multi-aperture imaging across the 8 regions in the vessel wall, paired t-tests performed. If the differences were not normally distributed, a paired Wilcoxon signed rank test was used. Differences were considered significant for $p < 0.05$.

3 Results

In 20 out of the 22 volunteers, the acquisition was performed without problems. The datasets of 2 volunteers were excluded,



because of a poor imaging window. The single-perspective and bistatic coherent dual-aperture ultrasound images of the abdominal aorta in 6 volunteers are visualized in **Figure 4**. It can be seen that using dual-aperture ultrasound imaging, a larger part of the vessel wall is visible. Moreover, in **Figure 5**, it is shown that the second transducer also enables a larger field-of-view. In **Figure 5A**, the vena cava was not visible because of acoustic shadowing. But in **Figure 5B**, the vena cava, the shape of the vertebra, and the abdominal muscles show improved visibility.

The vessel-lumen gCNR over all volunteers is quantified in **Figure 6**, which shows a significant increase of 0.16 ± 0.15 (40%) when using dual-aperture bistatic ultrasound imaging compared to single-perspective ultrasound, when considering the entire circumference of the aortic wall ($p < 10^{-8}$). When analyzing the 8 regions individually, it can be seen that the most information is added at the lateral sides of the single-perspective ultrasound configuration (R3 and R7) and at the vessel wall regions between the transducers (R4 and R8). In the latter regions, the reflections on the vessel wall originate from the trans-probe image data.

In R3, R4, R7, and R8, the mean increase in gCNR was equal to 0.27 ± 0.23 (78%). However, in R1 and R2, there was a small decrease in gCNR of -0.059 ± 0.20 (-8.6%) using bistatic imaging compared to single-perspective ultrasound. These regions correspond to the anterior part of the vessel wall that was also well visible in the single-perspective signal configuration. In the corresponding posterior part of the vessel wall (R5), the mean gCNR remained almost the same, comparing multi-aperture bistatic and single-perspective ultrasound, with a value of 0.57 ± 0.15 . The differences between single-perspective and multi-aperture bistatic imaging were significant in all regions except R5 ($p < 0.01$), which is indicated in **Figure 6**.

Similar results were found if the left probe was used for single-perspective imaging as a small decrease in gCNR of -0.096 ± 0.24 (-16%) was observed symmetrically in R6 and R7. However, the overall gCNR across the circumference of the aorta was also increased by 0.18 ± 0.15 (47%).

In each volunteer, the ultrasound images were acquired with different probe positions based on the best available imaging

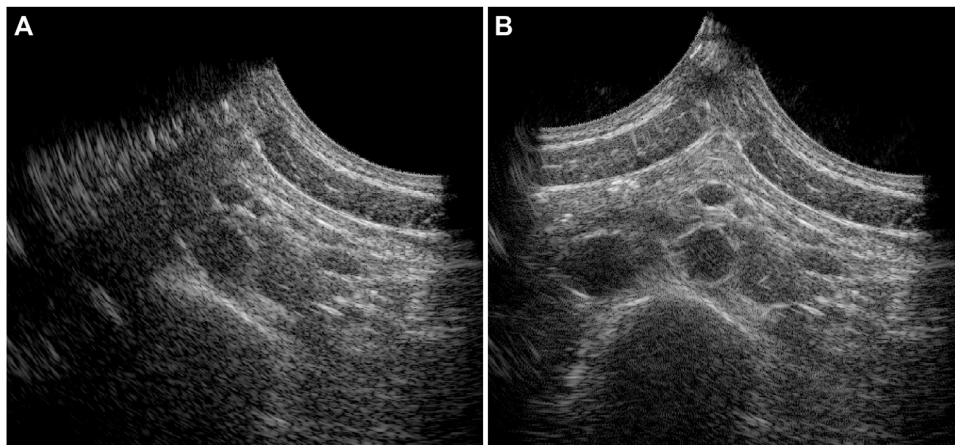


FIGURE 5 Full field-of-view images of the single-perspective (A) and bistatic dual-aperture ultrasound acquisitions (B) of the abdominal aorta in volunteer 1.

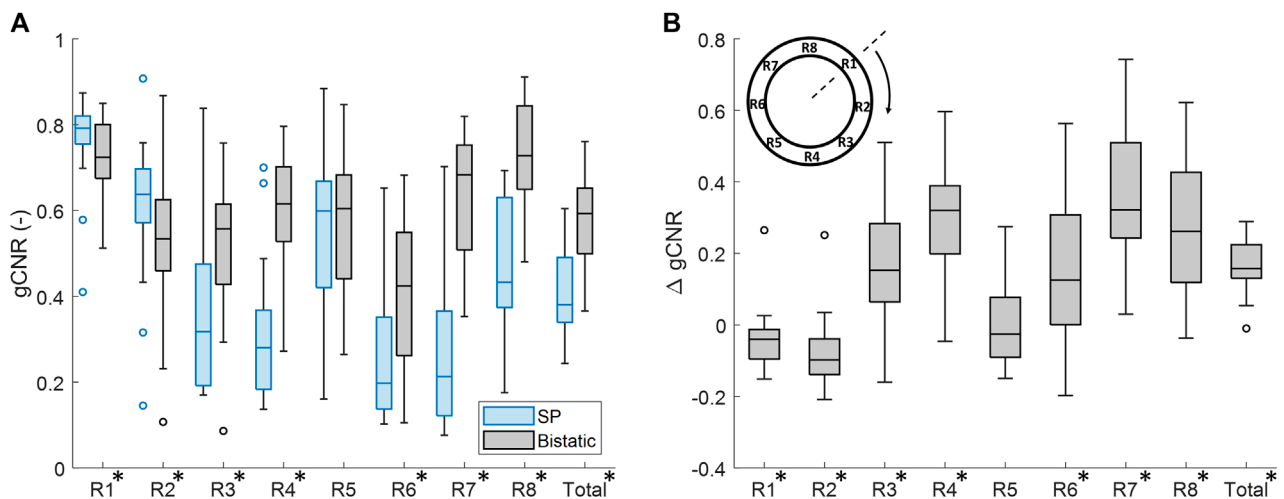
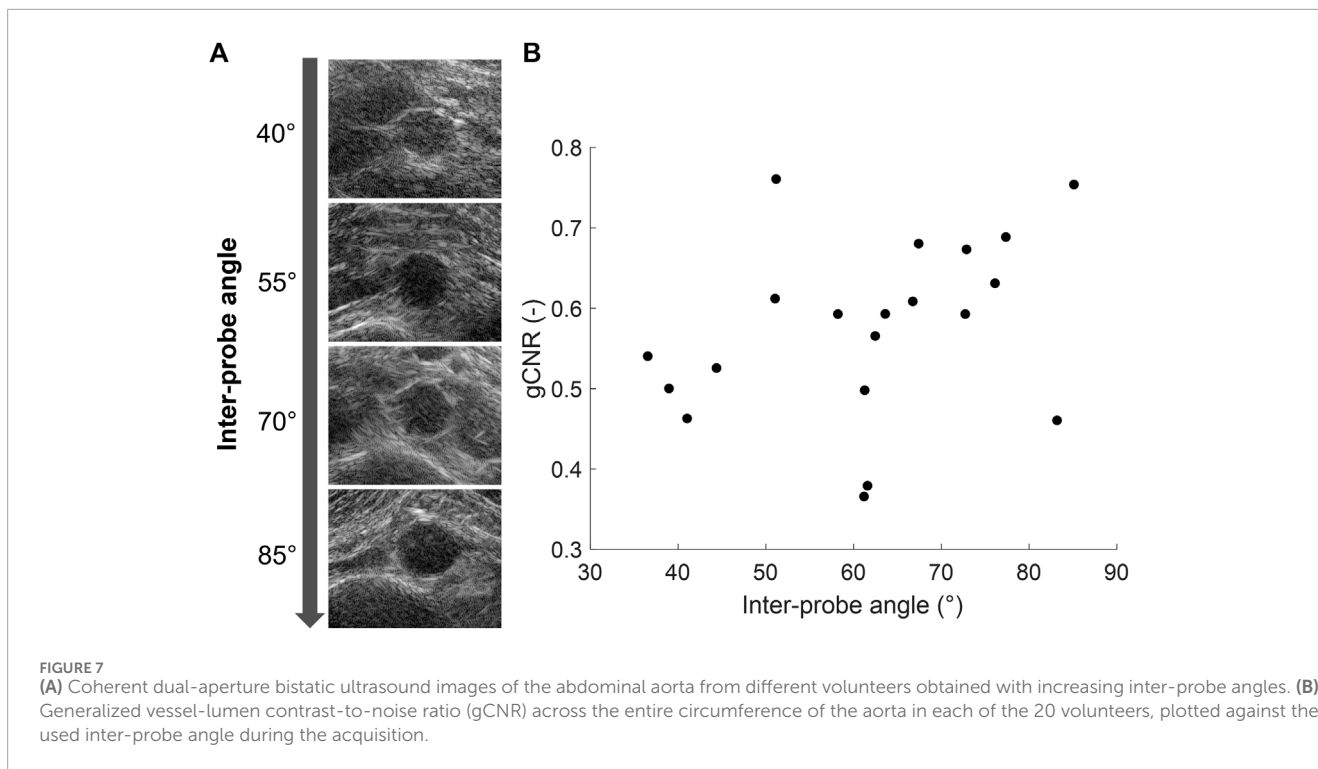


FIGURE 6 Regional analysis of the generalized contrast-to-noise ratio (gCNR) between the vessel wall and the lumen of the aorta in all volunteers. (A) gCNR in single-perspective (SP) and multi-aperture bistatic ultrasound imaging in the 8 regions of the vessel wall. (B) Difference in gCNR (Δ gCNR) for bistatic imaging compared to single-perspective ultrasound imaging. Regions in which the differences were statistically significant have been indicated with an asterisk in the label.

window. To investigate the influence of this relative probe positioning on the ultrasound image quality, the measured vessel-lumen gCNR in each volunteer was plotted against the used inter-probe angle during the acquisition in **Figure 7**. Here, it is shown that a larger vessel-lumen gCNR can be obtained when the ultrasound probes are positioned under an angle closer to 90°, since it results in a larger part of the vessel circumference to be visible by specular reflections. Next to the inter-probe angle, the gCNR also seemed to be dependent on the imaging depth, as higher gCNR values were obtained at smaller imaging depths. The two datasets with a large imaging depth (9 cm and 13 cm, respectively), and an inter-probe angle of around 60°, led to lower gCNRs of 0.37 and

0.38. However, in one dataset an inter-probe angle close to 85° also resulted in a relatively low gCNR of 0.46, despite the small imaging depth of 4.7 cm.

After performing fusion of the individual bistatic signals, functional imaging was performed. In **Figure 8**, the circumferential strain results at end-systole are shown for the same volunteers as in **Figure 4**. The estimation of local strains in the vessel wall using single-perspective ultrasound leads to a noisy pattern. However, by compounding the axial displacements from different directions, more homogeneous local strains are obtained, showing a high level of continuity without the use of regularization. Over all volunteers, a clear strain pattern is found with lower circumferential strains



at the posterior side, and higher circumferential strains at the anterior side. In some volunteers, like volunteer 7 (V7) and V16, the circumferential strains were also higher on the right side, compared to the left side because of the location of the spine.

In **Figure 9**, the radial strain pattern is shown corresponding to the examples in **Figure 8**. It is shown that the radial strain pattern becomes more homogeneous compared to the single-perspective imaging results. In some volunteers, like in V1 and V5, almost no radial strain was measured. However, in other volunteers, e.g., V7 and V16, lower radial strains were found at the anterior side of the vessel wall, and higher radial strains were found at the posterior side of the vessel wall.

By using multiple apertures, the overall mean tracking error was significantly reduced from $1.3 \text{ mm} \pm 0.63 \text{ mm}$ to $0.16 \text{ mm} \pm 0.076 \text{ mm}$, which is shown in **Figure 10** ($p < 10^{-4}$). In the regional analysis of the tracking error, it can be seen that the tracking error using bistatic ultrasound imaging was slightly larger in the anterior regions, compared to the posterior regions of the vessel wall. This is also related to the difference in expansion between the anterior and posterior side, as expansion of the vessel wall at the posterior side is limited by the spine.

In **Figure 11A**, it is shown that the overall mean $\text{SNRe}^{\text{circ}}$ was significantly increased by $12.3 \text{ dB} \pm 8.3 \text{ dB}$, using bistatic ultrasound imaging ($p < 10^{-5}$). Also when looking at each of the 8 regions individually, a significant increase in $\text{SNRe}^{\text{circ}}$ was observed using multi-aperture bistatic imaging compared to single-perspective imaging ($p < 0.01$).

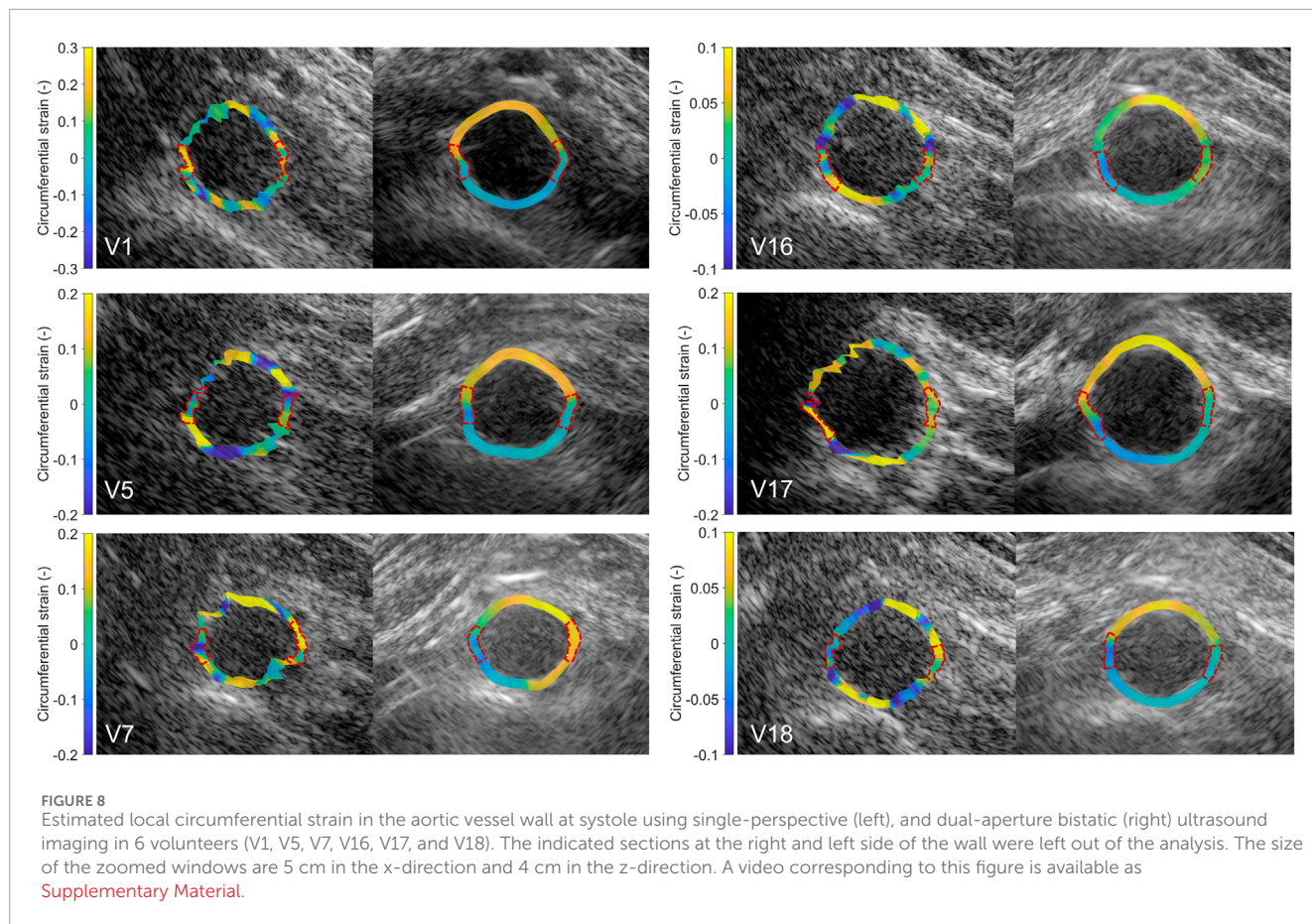
The change in SNRe^{rad} using bistatic ultrasound imaging compared to single-perspective ultrasound was not significant, except for R5, as shown in **Figure 11B**. In **Figure 9**, it can be seen that a certain amount variation inside the vessel wall remained after

displacement compounding. The largest increase in mean SNRe^{rad} was found in R1 and R5, by $5.3 \text{ dB} \pm 16.9 \text{ dB}$ and $6.6 \text{ dB} \pm 11.8 \text{ dB}$, respectively.

4 Discussion

In this study, the feasibility and performance of ultrafast dual-aperture bistatic ultrasound imaging and elastography of the abdominal aorta was tested for the first time *in vivo* on 20 healthy volunteers. It was shown that the 4 signals obtained with 2 transducers can be coherently compounded despite *in vivo* challenges, to create a better image of the abdominal aorta and its surroundings, *i.e.*, visualizing a larger part of the vessel wall with higher contrast. The addition of multidirectional high-resolution phase information also allows for improved local strain estimation because displacements can be estimated accurately in more directions.

The registration of the individual datasets was performed with the help of a customized arch, that allowed for read-out of the used probe angle. Optimization of the initial registration parameters could be performed fully automatically, without the use of inherent image features. Currently, an appropriate initialization was still necessary because multiple local minima could be found in the signal power of the trans-probe data. We also found out that in some cases, the global minimum did not correspond to the best alignment of the aorta, which is likely due to aberrations and artifacts involved. To improve the image quality by coherent compounding even more, aberration correction can be performed using for instance the methods presented in (Van Hal et al., 2023) or (Foiret et al., 2022). In the future, it might be possible to perform aberration correction and registration at the same time, since the correction for differences



in speed-of-sound also leads to better alignment of the imaged structures. This will also improve the resolution in the final bistatic ultrasound image even more, compared to the results shown in [Figures 4, 5](#), since improved coherence of the signals from multiple probes will lead to smaller point spread functions ([Foiret et al., 2022; Van Hal et al., 2023](#)). Future research could also focus on the optimization procedure to further automate this process, and to make it faster, since each gradient descent iteration required six reconstructions: two for each degree of freedom to be optimized.

Even without the use of aberration correction, this study has shown that the image quality and strain results were significantly improved compared to single-perspective ultrasound. The gCNR between the vessel wall and the lumen was found to increase by 40% on average, using bistatic ultrasound imaging compared to single-perspective ultrasound. Largest improvements were found at the lateral sides of the single-transducer configuration, i.e., R3 and R7, and also the vessel wall regions between the transducers, i.e., R4 and R8. However, in R1 and R2, which correspond to the anterior part of the vessel in the axial direction of the single-transducer configuration, there was a small decrease in vessel-lumen gCNR. This can be easily explained since these regions were already well visible in the single-perspective configuration. Hence, the added signals from the second transducer contributed less image information since R1, R2, and R5 correspond to its lateral direction where there is less contrast. In the future, smart compounding strategies can be investigated to further improve the coherent

compounded result. In ([Van Hal et al., 2021](#)), different weighted compounding strategies were tested that successfully optimized the vessel-lumen contrast. We also tested these strategies on the *in vivo* data, however, the used masks were not tailored to optimize the contrast in the surrounding tissues. Therefore, simple coherent compounding by [Eq. 3](#) was preferred to optimize the ultrasound image quality as a whole, at the cost of a slight decrease in gCNR in R1 and R2.

The resulting contrast of the abdominal aorta is dependent on both the imaging depth and the inter-probe angle. In general, an angle close to 90° between the transducers is desired since it results in a larger coverage of the vessel wall by specular reflections, as measured by the vessel-lumen gCNR, shown in [Figure 7](#). Of course in clinical practice, the optimal probe angle is mostly determined by the viewing window that depends on each patient's anatomy and for instance the presence of bowel gas. There was one case in which the gCNR was relatively low with a large probe angle and small imaging depth, which was not expected. In this dataset, the trans-probe signals appeared as blurred, and also affected the strain estimation in the vessel wall regions between the transducers. This implies that for widespread clinical use, a multi-aperture array with sufficient degrees-of-freedom combined with shape sensing may be required to ensure high inclusion rates and the most optimal improvements in image quality. Finally, bistatic multi-aperture ultrasound images may also benefit from some post-processing as commonly performed on most modern clinical ultrasound systems,

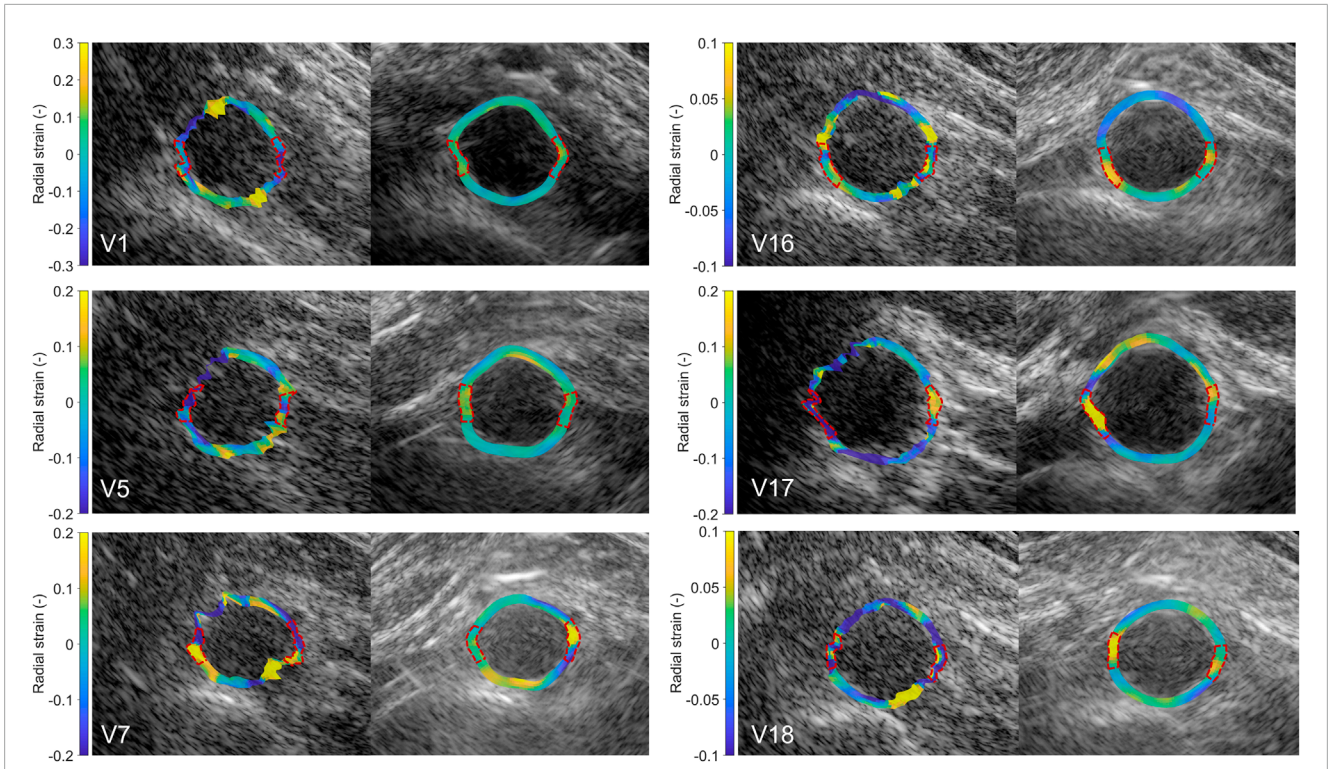


FIGURE 9 Estimated local radial strain in the aortic vessel wall at systole using single-perspective (left), and dual-aperture bistatic (right) ultrasound imaging in 6 volunteers (V1, V5, V7, V16, V17, and V18). The indicated sections at the right and left side of the wall were left out of the analysis. The size of the zoomed windows are 5 cm in the x-direction and 4 cm in the z-direction. A video corresponding to this figure is available as [Supplementary Material](#).

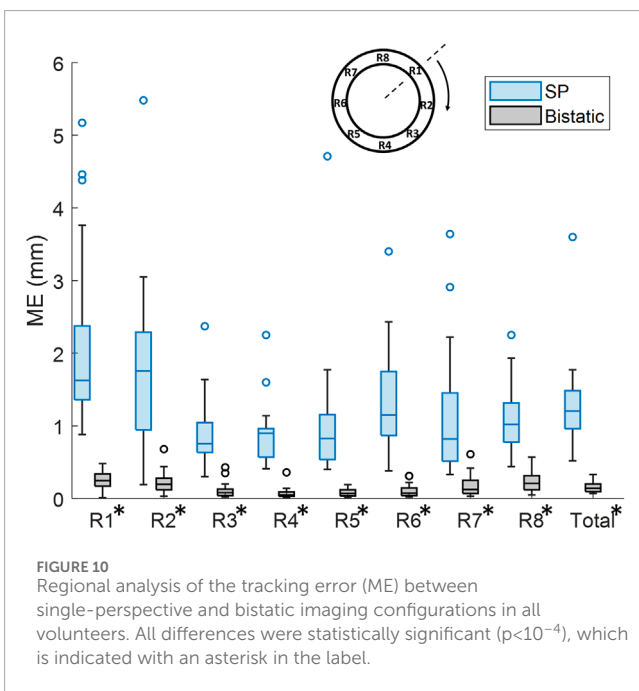


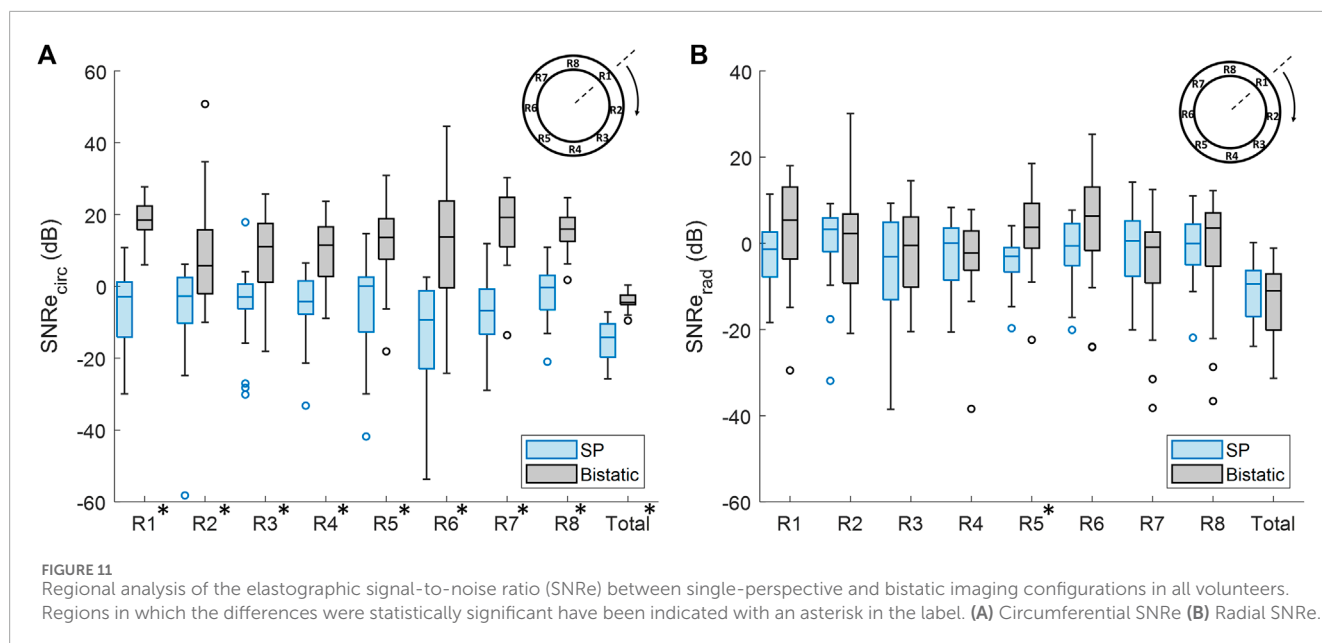
FIGURE 10 Regional analysis of the tracking error (ME) between single-perspective and bistatic imaging configurations in all volunteers. All differences were statistically significant ($p < 10^{-4}$), which is indicated with an asterisk in the label.

to ensure that the image quality meets the clinician’s preferences. The results in shown in [Figures 4, 5](#) present “raw” ultrasound images, meaning that no additional filtering is applied. This is done

to ensure a fair quantitative comparison of the employed image quality metrics.

The *in vivo* strain imaging results showed that local strain estimation using single-perspective ultrasound is extremely difficult, because of the large imaging depth combined with the small wall thickness, in line with our previous *ex vivo* findings ([Van Hal et al., 2021](#); [De Hoop et al., 2020](#)). The displacements can only be accurately determined in the axial direction of the ultrasound probe, while in the lateral direction motion drift is present. By using a second aperture, the displacements can be estimated accurately in more directions and by applying angular weighted displacement compounding, a homogeneous strain pattern can be obtained which resulted in an increase of overall circumferential SNR_{e}^{circ} by $12.3 \text{ dB} \pm 8.3 \text{ dB}$. In the left and the right wall, small sections between 35° and 40° wide were left out of the analysis in both single-perspective and multi-aperture bistatic imaging, since these regions could still not be well visualized using the current set-up. As a result, less accurate strain estimates were obtained in these regions using bistatic imaging, similar to the single probe estimations. In the future, this can be resolved with an even larger aperture.

In this study, a coarse-to-fine, block-matching based speckle tracking algorithm was used to obtain the 2D displacement fields. Future implementation of multi-aperture bistatic imaging could potentially benefit from more advanced tracking algorithms, like [Jiang and Hall \(2011\)](#), which could improve the strain estimation results even more. This was out of the scope of the current study to isolate the comparison of single and multi-aperture imaging from



other effects as much as possible. Moreover, this study has shown that using bistatic imaging, strain estimation can be improved by nature, without the use of any regularization.

In R1, R2, and R5 large improvements in motion tracking and $\text{SNRe}^{\text{circ}}$ were obtained despite the similar or slightly decreased gCNR. In these regions, the circumferential direction is aligned with the lateral direction in the single-perspective imaging configuration. In the single-perspective results, no radial displacement projection was performed, hence, the large tracking errors and low $\text{SNRe}^{\text{circ}}$ can be explained by lateral motion drift. This lateral motion drift was even worse compared to for instance R3, since R3 contained more image information in the lateral direction. In dual-aperture imaging, displacement compounding could be performed using only the estimated axial displacements from different angles, leaving out the erroneous lateral displacements. Therefore, the lateral motion drift present in the single-perspective configuration could be mitigated, which exhibited improved displacement estimation across the entire circumference of the aorta.

The resulting circumferential strain pattern using bistatic ultrasound imaging showed a clear distinction in magnitude between the anterior and posterior side of the vessel wall, that was not visible using single-perspective ultrasound imaging. This can be explained by the fact that the expansion of the aorta at the posterior side is limited by the presence of the spine and branching lumbar arteries (Goergen et al., 2007). However, in some volunteers, the circumferential strain at the posterior side was negative, which was not expected, although it is in accordance with findings from other literature (Karatolios et al., 2013; Taniguchi et al., 2014; Bracco et al., 2023). Comparing the bistatic strain patterns of V7, V16, and V18 against the single-perspective results, it may seem like the single-perspective strains in the posterior wall are more reasonable (positive circumferential strains, and negative radial strains). However, the lateral motion drift present in the single-perspective imaging configuration (as characterized by the mean error) causes overestimation (V7, V16, and V18) and underestimation (V5) as mesh nodes move toward

or away of each other as a result of the accumulation of errors in the displacement estimates. The single-perspective strain results are therefore less accurate compared to the bistatic strain results. Negative circumferential strains accompanied by radial expansion, like estimated in V7, may be physiological. Otherwise, these results could be explained by incorrect assumptions in the displacement model, and out-of-plane motion. It is important to note that the estimation of local displacements was performed with respect to a fixed reference frame and midpoint. In future research, it could be more accurate to take the change in local radial and circumferential directions during the cardiac cycle into account.

The estimation of radial strain within the vessel wall still proved to be challenging. The radial strain pattern was often not homogeneous within the wall, which still resulted in similar SNRe^{rad} compared to the single-perspective results. However, especially in V16, some correspondence with the circumferential strain results was found, as visualized in Figures 8, 9. Here, it can be seen that more negative radial strains correspond with positive circumferential strains at the anterior side of the vessel wall, and lower strains are found at the posterior side of the vessel wall. The radial strains are likely less accurate compared to the circumferential strains because of the relatively low center frequency of the transducer (3.7 MHz), which limits the axial resolution (which even worsens at lower depths), combined with the small wall thickness (1.7 mm). Therefore, the difference in movement between the inner and outer wall is harder to distinguish. Moreover, the expected thinning of the aortic wall is in the same order of magnitude as the measured tracking error, which limits the precision of the radial strain estimates.

The *in vivo* strain results were limited by the lack of a ground truth. In previous research (Van Hal et al., 2021), bistatic multi-aperture strain imaging results showed good agreement with the ground truth strain obtained from ultrasound simulations. In the future, more realistic ultrasound simulations based on biomechanical models could help to fully validate *in vivo* strain patterns, incorporating *in vivo* wall geometries and properties

to mimic the inhomogeneous deformation (Van Disseldorp et al., 2019; Bracco et al., 2023).

The current study was performed in healthy volunteers to show the feasibility and performance of multi-aperture bistatic ultrasound imaging and elastography *in vivo*. As a next step, the methods can be validated in AAA patients gradually moving towards the final application. In the future, we also envision a more flexible set-up, rather than the currently used experimental arch, for instance using probe holders with multiple apertures attached Zimmer et al. (2023). This will still allow for the clinician to perform a free-hand scan, and use 3-D ultrasound. These developments could in the future also contribute towards semi-tomographic ultrasound approaches that can cover a large FOV, for instance using wearable ultrasound patches (Lin et al., 2023). 3-D bistatic ultrasound imaging using two sparse matrix arrays has recently been proven feasible in an *ex vivo* study (De Hoop et al., 2022). This removes the limitation of scanning in the same imaging plane and can capture out-of-plane motion.

5 Conclusion

Multi-aperture ultrasound imaging and elastography and its feasibility *in vivo* was shown. This novel ultrasound modality can provide the clinician with much needed information about the geometry and mechanical state of the aortic wall. Using bistatic multi-aperture ultrasound imaging, both the contrast and resolution of the ultrasound images can be improved which enables accurate estimation of local motion dynamics and strain in the abdominal aortic wall. Future *in vivo* studies will focus on the practical application of multi-aperture acquisition in the clinic, in patients with AAAs, and extending our approach to full 3-D ultrasound which will allow for more free-hand operation.

Data availability statement

The datasets presented in this article are not readily available due to ethical restrictions. Requests to access the datasets should be directed to v.h.j.v.hal@tue.nl or r.lopata@tue.nl.

Ethics statement

The studies involving humans were approved by the Ethical Review Board of the Eindhoven University of Technology. The studies were conducted in accordance with the local legislation and institutional requirements. The participants provided their written informed consent to participate in this study.

References

Alomari, Z., Harput, S., Hyder, S., and Freear, S. (2014). "Selecting the number and values of the CPWI steering angles and the effect of that on imaging quality," in 2014 IEEE International Ultrasonics Symposium (IEEE), Chicago, IL, USA, 03-06 September 2014, 1191–1194.

Author contributions

VH: Conceptualization, Data curation, Formal Analysis, Investigation, Methodology, Software, Validation, Visualization, Writing—original draft. HH: Methodology, Software, Writing—review and editing. MS: Supervision, Writing—review and editing. H-MS: Conceptualization, Methodology, Software, Supervision, Writing—review and editing. RL: Conceptualization, Funding acquisition, Methodology, Project administration, Resources, Supervision, Writing—review and editing.

Funding

The author(s) declare financial support was received for the research, authorship, and/or publication of this article. This work was supported by the Dutch Research Council (NWO) and received funding from the NWO talent program VIDI (17533, awarded to RL).

Acknowledgments

The authors would like to thank J. A. Bulsink for the construction of the mechanical arch and the customized probe holders used for the ultrasound acquisitions.

Conflict of interest

The authors declare that the research was conducted in the absence of any commercial or financial relationships that could be construed as a potential conflict of interest.

Publisher's note

All claims expressed in this article are solely those of the authors and do not necessarily represent those of their affiliated organizations, or those of the publisher, the editors and the reviewers. Any product that may be evaluated in this article, or claim that may be made by its manufacturer, is not guaranteed or endorsed by the publisher.

Supplementary material

The Supplementary Material for this article can be found online at: <https://www.frontiersin.org/articles/10.3389/fphys.2024.1320456/full#supplementary-material>

Bihari, P., Shelke, A., Nwe, T. H., Mularczyk, M., Nelson, K., Schmandra, T., et al. (2013). Strain measurement of abdominal aortic aneurysm with real-time 3D ultrasound speckle tracking. *Eur. J. Vasc. Endovasc. Surg.* 45, 315–323. doi:10.1016/j.ejvs.2013.01.004

- Bracco, M. I., Broda, M., Lorenzen, U. S., Florkow, M. C., Somphone, O., Avril, S., et al. (2023). Fast strain mapping in abdominal aortic aneurysm wall reveals heterogeneous patterns. *Front. Physiology* 14, 1163204. doi:10.3389/fphys.2023.1163204
- Brewster, D. C., Cronenwett, J. L., Hallett, J. W., Johnston, K., Krupski, W. C., Matsumura, J. S., et al. (2003). Guidelines for the treatment of abdominal aortic aneurysms: report of a subcommittee of the joint council of the american association for vascular surgery and society for vascular surgery. *J. Vasc. Surg.* 37, 1106–1117. doi:10.1067/mva.2003.363
- Burkholder, R., Gupta, L., and Johnson, J. (2003). Comparison of monostatic and bistatic radar images. *IEEE Antennas Propag. Mag.* 45, 41–50. doi:10.1109/map.2003.1232162
- Céspedes, I., Huang, Y., Ophir, J., and Spratt, S. (1995). Methods for estimation of subsample time delays of digitized echo signals. *Ultrason. Imaging* 17, 142–171. doi:10.1177/016173469501700204
- Darling, R., Messina, C., Brewster, D., and Ottinger, L. (1977). Autopsy study of unoperated abdominal aortic aneurysms. the case for early resection. *Circulation* 56, II161–II164.
- De Hoop, H., Petterson, N. J., van de Vosse, F. N., van Sambeek, M. R. H. M., Schwab, H.-M., and Lopata, R. G. P. (2020). Multiperspective ultrasound strain imaging of the abdominal aorta. *IEEE Trans. Med. Imag.* 39, 3714–3724. doi:10.1109/TMI.2020.3003430
- De Hoop, H., Vermeulen, M., Schwab, H.-M., and Lopata, R. G. (2022). Coherent bistatic 3-d ultrasound imaging using two sparse matrix arrays. *IEEE Trans. Ultrasonics, Ferroelectr. Freq. Control* 70, 182–196. doi:10.1109/TUFFC.2022.3233158
- Devaney, A. J. (2012). *Mathematical foundations of imaging, tomography and wavefield inversion*. Cambridge: Cambridge University Press.
- Dunmire, B., Beach, K., Labs, K., Plett, M., and Strandness, D., Jr (2000). Cross-beam vector Doppler ultrasound for angle-independent velocity measurements. *Ultrasound Med. Biol.* 26, 1213–1235. doi:10.1016/s0301-5629(00)00287-8
- Foiret, J., Cai, X., Bendjador, H., Park, E.-Y., Kamaya, A., and Ferrara, K. W. (2022). Improving plane wave ultrasound imaging through real-time beamformation across multiple arrays. *Sci. Rep.* 12, 13386. doi:10.1038/s41598-022-16961-2
- Goergen, C. J., Johnson, B. L., Greve, J. M., Taylor, C. A., and Zarins, C. K. (2007). Increased anterior abdominal aortic wall motion: possible role in aneurysm pathogenesis and design of endovascular devices. *J. Endovascular Ther.* 14, 574–584. doi:10.1177/152660280701400421
- Hansen, H. H. G., Lopata, R. G. P., Idzenga, T., and de Korte, C. L. (2010). An angular compounding technique using displacement projection for noninvasive ultrasound strain imaging of vessel cross-sections. *Ultrasound Med. Biol.* 36, 1947–1956. doi:10.1016/j.ultrasmedbio.2010.06.008
- Jiang, J., and Hall, T. J. (2011). A fast hybrid algorithm combining regularized motion tracking and predictive search for reducing the occurrence of large displacement errors. *IEEE Trans. Ultrasonics, Ferroelectr. Freq. Control* 58, 730–736. doi:10.1109/TUFFC.2011.1865
- Karatolios, K., Wittek, A., Nwe, T. H., Bihari, P., Shelke, A., Josef, D., et al. (2013). Method for aortic wall strain measurement with three-dimensional ultrasound speckle tracking and fitted finite element analysis. *Ann. Thorac. Surg.* 96, 1664–1671. doi:10.1016/j.athoracsur.2013.06.037
- Lin, M., Zhang, Z., Gao, X., Bian, Y., Wu, R. S., Park, G., et al. (2023). A fully integrated wearable ultrasound system to monitor deep tissues in moving subjects. *Nat. Biotechnol.* 2023, 1–10. doi:10.1038/s41587-023-01800-0
- Liu, P., de Hoop, H., Schwab, H.-M., and Lopata, R. G. (2022a). High frame rate multi-perspective cardiac ultrasound imaging using phased array probes. *Ultrasonics* 123, 106701. doi:10.1016/j.ultras.2022.106701
- Liu, P., Muller, J.-W., Schwab, H.-M., and Lopata, R. (2022b). Cardiac strain imaging using multi-perspective ultrafast ultrasound. *Front. Phys.* 10, 119. doi:10.3389/fphys.2022.789263
- Lopata, R. G. P., Hansen, H. H. G., Nillesen, M. M., Thijssen, J. M., and De Korte, C. L. (2009a). Comparison of one-dimensional and two-dimensional least-squares strain estimators for phased array displacement data. *Ultrason. Imaging* 31, 1–16. doi:10.1177/016173460903100101
- Lopata, R. G. P., Nillesen, M. M., Hansen, H. H. G., Gerrits, I. H., Thijssen, J. M., and de Korte, C. L. (2009b). Performance evaluation of methods for two-dimensional displacement and strain estimation using ultrasound radio frequency data. *Ultrasound Med. Biol.* 35, 796–812. doi:10.1016/j.ultrasmedbio.2008.11.002
- Matthews, E. O., Pinchbeck, J., Elmore, K., Jones, R. E., Moxon, J. V., and Gollgedge, J. (2021). The reproducibility of measuring maximum abdominal aortic aneurysm diameter from ultrasound images. *Ultrasound J.* 13, 13–16. doi:10.1186/s13089-021-00211-z
- Mulder, H. W., van Stralen, M., van der Zwaan, H. B., Leung, K. E., Bosch, J. G., and Pluim, J. P. (2014). Multiframe registration of real-time three-dimensional echocardiography time series. *J. Med. Imaging* 1, 014004. doi:10.1117/1.JMI.1.1.014004
- NEN-EN-IEC 60601-2-37:2008/A1:2015 (2015). *Medical electrical equipment - Part 2-37: particular requirements for the basic safety and essential performance of ultrasonic medical diagnostic and monitoring equipment*. Netherlands: Standard, Nederlands Normalisatie Instituut.
- Peralta, L., Gomez, A., Luan, Y., Kim, B.-H., Hajnal, J. V., and Eckersley, R. J. (2019). Coherent multi-transducer ultrasound imaging. *IEEE Trans. Ultrason. Ferroelectr. Freq. Control* 66, 1316–1330. doi:10.1109/TUFFC.2019.2921103
- Peralta, L., Zimmer, V. A., Christensen-Jeffries, K., Ramalli, A., Skelton, E., Matthew, J., et al. (2020). “Coherent multi-transducer ultrasound imaging: first *in vivo* results,” in 2020 IEEE International Ultrasonics Symposium (IUS) (IEEE), Las Vegas, NV, USA, 07–11 September 2020, 1–4.
- Petterson, N. J., van Sambeek, M. R. H. M., van de Vosse, F. N., and Lopata, R. G. P. (2021). Enhancing lateral contrast using multi-perspective ultrasound imaging of abdominal aortas. *Ultrasound Med. Biol.* 47, 535–545. doi:10.1016/j.ultrasmedbio.2020.09.023
- Rajpoot, K., Grau, V., Noble, J. A., Szmigielski, C., and Becher, H. (2011). Multiview fusion 3-d echocardiography: improving the information and quality of real-time 3-d echocardiography. *Ultrasound Med. Biol.* 37, 1056–1072. doi:10.1016/j.ultrasmedbio.2011.04.018
- Raut, S. S., Chandra, S., Shum, J., and Finol, E. A. (2013). The role of geometric and biomechanical factors in abdominal aortic aneurysm rupture risk assessment. *Ann. Biomed. Eng.* 41, 1459–1477. doi:10.1007/s10439-013-0786-6
- Rodriguez-Molares, A., Rindal, O. M. H., D’hooge, J., Måsøy, S.-E., Austeng, A., Bell, M. A. L., et al. (2019). The generalized contrast-to-noise ratio: a formal definition for lesion detectability. *IEEE Trans. Ultrasonics, Ferroelectr. Freq. Control* 67, 745–759. doi:10.1109/TUFFC.2019.2956855
- Sjoerdsma, M., Verstraeten, S. C., Maas, E. J., van de Vosse, F. N., van Sambeek, M. R., and Lopata, R. G. (2023). Spatiotemporal registration of 3-d multi-perspective ultrasound images of abdominal aortic aneurysms. *Ultrasound Med. Biol.* 49, 318–332. doi:10.1016/j.ultrasmedbio.2022.09.005
- Slobodin, G., Nakhleh, A., Rimar, D., Wolfson, V., Rosner, I., and Odeh, M. (2016). Increased aortic wall thickness for the diagnosis of aortitis: a computed tomography-based study. *Int. J. Rheumatic Dis.* 19, 82–86. doi:10.1111/1756-185X.12742
- Taniguchi, R., Hoshina, K., Hosaka, A., Miyahara, T., Okamoto, H., Shigematsu, K., et al. (2014). Strain analysis of wall motion in abdominal aortic aneurysms. *Ann. Vasc. Dis.* 7, 393–398. doi:10.3400/avd.0a.14-00067
- Tanter, M., and Fink, M. (2014). Ultrafast imaging in biomedical ultrasound. *IEEE Trans. Ultrason. Ferroelectr. Freq. Control* 61, 102–119. doi:10.1109/TUFFC.2014.6689779
- Techavipoo, U., Chen, Q., Varghese, T., and Zagzebski, J. A. (2004). Estimation of displacement vectors and strain tensors in elastography using angular insonifications. *IEEE Trans. Med. Imaging* 23, 1479–1489. doi:10.1109/TMI.2004.835604
- Van Disseldorp, E. M., Petterson, N. J., van de Vosse, F. N., van Sambeek, M. R., and Lopata, R. G. (2019). Quantification of aortic stiffness and wall stress in healthy volunteers and abdominal aortic aneurysm patients using time-resolved 3d ultrasound: a comparison study. *Eur. Heart Journal-Cardiovascular Imaging* 20, 185–191. doi:10.1093/ehjci/jey051
- Van Disseldorp, E. M. J., Petterson, N. J., Rutten, M. C. M., van de Vosse, F. N., van Sambeek, M. R. H. M., and Lopata, R. G. P. (2016). Patient specific wall stress analysis and mechanical characterization of abdominal aortic aneurysms using 4D ultrasound. *Eur. J. Vasc. Endovasc. Surg.* 52, 635–642. doi:10.1016/j.ejvs.2016.07.088
- Van Hal, V. H. J., De Hoop, H., Muller, J.-W., van Sambeek, M. R. H. M., Schwab, H.-M., and Lopata, R. G. P. (2021). Multiperspective bistatic ultrasound imaging and elastography of the *ex vivo* abdominal aorta. *IEEE Trans. Ultrasonics, Ferroelectr. Freq. Control* 69, 604–616. doi:10.1109/TUFFC.2021.3128227
- Van Hal, V. H. J., Muller, J.-W., Van Sambeek, M. R. H. M., Lopata, R. G. P., and Schwab, H.-M. (2023). An aberration correction approach for single and dual aperture ultrasound imaging of the abdomen. *Ultrasonics* 131, 106936. doi:10.1016/j.ultras.2023.106936
- Wanhainen, A., Verzini, F., Van Herzele, I., Allaire, E., Bown, M., Cohnert, T., et al. (2020). Corrigendum to: European society for vascular surgery (ESVS) 2019 clinical practice guidelines on the management of abdominal aortoiliac artery aneurysms. *Eur. J. Vasc. Endovasc. Surg.* 59, 494. doi:10.1016/j.ejvs.2019.11.026
- Wittek, A., Karatolios, K., Bihari, P., Schmitz-Rixen, T., Moosdorf, R., Vogt, S., et al. (2013). *In vivo* determination of elastic properties of the human aorta based on 4D ultrasound data. *J. Mech. Behav. Biomed. Mater.* 27, 167–183. doi:10.1016/j.jmbbm.2013.03.014
- Zimmer, V. A., Gomez, A., Skelton, E., Wright, R., Wheeler, G., Deng, S., et al. (2023). Placenta segmentation in ultrasound imaging: addressing sources of uncertainty and limited field-of-view. *Med. Image Anal.* 83, 102639. doi:10.1016/j.media.2022.102639